Mechanics of Materials 91 (2015) 313–322

Contents lists available at ScienceDirect

Mechanics of Materials

journal homepage: www.elsevier.com/locate/mechmat

Lithiation of ZnO nanowires studied by *in-situ* transmission electron microscopy and theoretical analysis

Yuefei Zhang [a], Zhenyu Wang [a], Yujie Li [a], Kejie Zhao [b,*]

[a] Institute of Microstructure and Property of Advanced Materials, Beijing University of Technology, Beijing 100124, PR China
[b] School of Mechanical Engineering, Purdue University, West Lafayette, IN 47906, USA

ARTICLE INFO

Article history:
Received 30 December 2014
Received in revised form 15 February 2015
Available online 14 May 2015

Keywords:
Li-ion batteries
ZnO
Stress
Oxides
Fracture

ABSTRACT

Transition-metal oxides constitute an important family of high-capacity anodes for Li-ion batteries. ZnO is a model material due to the high theoretical capacity and its representative reaction mechanism upon lithiation. We investigate the structural evolution, mechanical degradation, and stress-regulated electrochemical reactions of ZnO nanowires during the first lithiation through coordinated *in-situ* transmission electron microcopy experiments, continuum theories, and first-principles computation. Lithiation induces a field of stress in ZnO nanowires. The stress field mediates the electrochemical reaction and breaks the planar solid-state reaction front into a curved interface. The tensile stress in the lithiated shell causes surface fracture in the basal plane of nanowires. The compressive stress in the unlithiated core retards local reactions and results in an uneven lithiation on a given basal plane. We also observe that metallic Zn nanoparticles aggregate in the amorphous matrix of the reaction products. At a critical size, Zn nanoparticles impede the propagation of the reaction front due to the thermodynamically unfavorable lithiation reaction. The results provide fundamental perspectives on the chemomechanical behaviors of oxides for the next-generation Li-ion batteries.

1. Introduction

Li-ion batteries are ubiquitous in the market of portable electronics and are being implemented to power electric vehicles (Service, 2014; Van Noorden, 2014). The imperative demand of high-energy–density batteries stimulated intensive search on the high-capacity electrodes over the past decades (Yu et al., 2014). Metal oxides, such as SiO_2, TiO_2, ZnO, SnO_2, Co_3O_4, and Fe_2O_3/Fe_3O_4, constitute an important family for high-capacity electrodes (Jiang et al., 2012; Huang et al., 2010; Favors et al., 2014; Tao et al., 2012; Zhang et al., 2014a,b). They typically have a theoretical capacity on the order of 1000 mAh/g which is about three times higher than the conventional graphite anodes. Among these materials, ZnO is a model system due to its high theoretical capacity and the typical reaction mechanism upon lithiation. ZnO undergoes a two-step reaction during lithiation (Li et al., 1999). Li first converts the oxide into metallic Zn and Li_2O, $ZnO + 2Li^+ + 2e^- \leftrightarrow Li_2O + Zn$, then Li alloys with Zn to form different Li–Zn compounds, $Zn + xLi^+ + xe^- \leftrightarrow Li_xZn$. The irreversible capacity loss of oxide anodes is mainly attributed to the first conversion reaction, while the deliverable capacity in the subsequent cycles is due to the second alloying reaction. However, the detailed pathway and the fundamental mechanism at the intrinsic scale of the electrochemical reactions remain elusive. Equipped with *in-situ* transmission electron microscopy (TEM) using a single ZnO nanowire as the working electrode, we unravel the microstructural evolution at an unprecedented spatial and temporal resolution. We observe that metallic Zn nanoparticles aggregate in the

* Corresponding author. Tel.: +1 765 496 0224.
E-mail address: kjzhao@purdue.edu (K. Zhao).

http://dx.doi.org/10.1016/j.mechmat.2015.05.004
0167-6636/

amorphous matrix of the reaction products. At a critical size, Zn nanoparticles impede the propagation of the reaction front due to the thermodynamically unfavorable lithiation reaction.

In addition, ZnO provides an example to study the intimate coupling between mechanics and electrochemistry. Lithiation causes a volumetric strain of ~100% in ZnO (Kushima et al., 2011). Such a large deformation induces a field stress, which leads to fracture and drastic morphological changes. The mechanical degradation driven by the electrochemical process of Li insertion and extraction is inherent to high-capacity electrodes and often leads to rapid capacity loss in the first few cycles (Zhang, 2011; Zhao et al., 2011, 2012; Wan et al., 2014). Meanwhile, mechanics influences the chemistry of lithiation in a significant manner. Stress affects reactions at the interface between the electrode and electrolyte, the propagation of solid–solid reaction front, diffusion of Li in electrode particles, and phase transformations of electrode materials (Yang et al., 2014; Zhao et al., 2012; Haftbaradaran et al., 2010; Pharr et al., 2012; Tang et al., 2011; McDowell et al., 2012). In ZnO, we demonstrate discrete surface cracks induced by tensile stresses in the lithiated shell. The fracture surfaces provide fast channels for Li penetration that ultimately divides the nanowires into multiple segments of nanoglass domains (Kushima et al., 2011). The compressive stress in the unlithiated core, on the other hand, causes retardation of local electrochemical reaction and results in a cross-sectionally uneven lithiation. Lithiation also results in significant embrittlement of the oxide nanowire and leads to a transition from a pristine material with resilient elasticity to a fragile structure in the lithiated form.

The overall picture of characteristics in lithiation of ZnO nanowires is depicted in Fig. 1. Once a reliable contact is made between a single ZnO nanowire with the counter electrode and the electrolyte Li/Li_2O, Li ions diffuse quickly on the nanowire surface, forming a thin wetting layer with typical thickness of a few nanometers. The nanowire is first lithiated radially and the extent of lithiation is limited by the amount of Li transport through the thin wetting layer. The solid-state reaction front (SSRF) primarily propagates along the longitudinal direction of the nanowire away from the electrolyte. The radial lithiation forms a structure of lithiated shell and unlithiated core. A field of stress is associated with the core–shell geometry (Zhao et al., 2012). While the tensile stress in the lithiated shell induces discrete surface cracks and facilitates Li transport through the crack surfaces, the compressive stress in the pristine core diminishes the thermodynamic driving force of the electrochemical reaction and impedes the local lithiation. The asymmetry of the characteristic stresses breaks the planar SSRF into a curved interface that is a reminiscence of Mullins–Sekerka interfacial instability (Mullins and Sekerka, 1964). In addition, metallic Zn nanoparticles aggregate in the amorphous matrix during the conversion reaction. The size of these nanoparticles steadily increases in the course of lithiation. The metallic phase largely blocks the path of Li transport at a critical size, and reduces the propagation velocity of the SSRF due to the thermodynamically unfavorable reaction with Li. These salient features will be elaborated in great detail in the following sections.

2. Experimental procedures

2.1. Material synthesis and characterization

ZnO nanowires with the growth orientation [0001] were prepared on a Si (001) substrate by the hollow-cathode discharge plasma chemical vapor deposition method. During the process, Ar was used as the plasma forming gas, O_2 as the reactive gas, and metal zinc powder (99.99% purity) vaporized by plasma heating over 1100 °C as the zinc source. Details of the growth process and the optimum conditions to obtain high-purity nanowires were reported elsewhere (Bian et al., 2008; Chunqing et al., 2009). High-resolution transmission electron microscopy (HRTEM) was conducted using a JEOL-2010 TEM operated at 200 kV. The chemical composition of the samples was detected using energy dispersive X-ray spectroscopy (EDS, Oxford Instruments). The surface and morphology were imaged using a scanning electron microscopy (SEM, FEI Quanta 250, and JEOL 6500F). Individual ZnO nanowires were fully characterized using SEM, HRTEM, and energy dispersive X-ray (EDX) spectroscopy prior to starting the measurements on the electrochemical and mechanical properties. Fig. 2(a) shows a SEM image of as-synthesized ZnO nanowires. The diameters are in between 80 and 500 nm, and the length is typically a few micrometers. Fig. 2(b) shows the wurtzite structure of individual crystalline nanowires. A

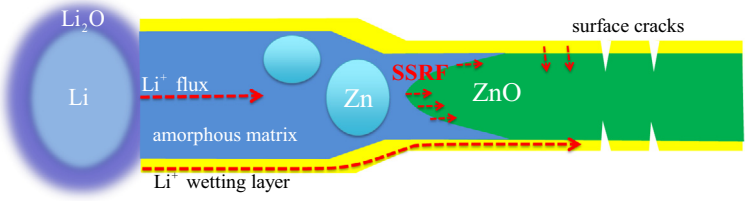

Fig. 1. Schematic illustration of the overall features of lithiation in ZnO nanowires. Li ions diffuse quickly on the nanowire surface, forming a thin wetting layer with typical thickness of a few nanometers. The nanowire surface is first lithiated and the extent of lithiation is limited by Li transport through the thin wetting layer. The primary solid-state reaction front (SSRF) propagates along the longitudinal direction of the nanowire away from the electrolyte. Metallic Zn nanoparticles aggregate in the amorphous matrix of the reaction products. At a critical size, Zn nanoparticles impede the propagation of the reaction front. Lithiation induces a field of tensile stress in the lithiated shell, and compressive stress in the unlithiated core. The tensile stress causes surface fracture in the (0001) basal plane of ZnO nanowires. The stress field regulates the lithiation reaction and breaks the planar SSRF into a curved interface.

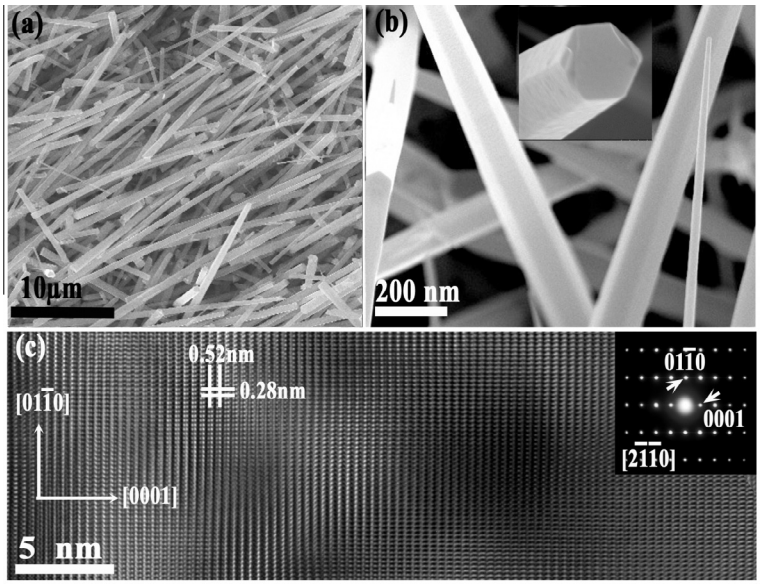

Fig. 2. (a) A SEM image of as-synthesized ZnO nanowires. The diameters are in between 80 and 500 nm, and the length is typically a few micrometers. (b) The wurtzite structure of individual crystalline ZnO nanowires. (c) A HRTEM image shows the atomistic structure of pristine ZnO nanowires. The image is viewed from the $[2\bar{1}\bar{1}0]$ direction. The inset SAED pattern indicates the [0001] growth direction of the nanowires.

high-resolution TEM image in Fig. 2(c) further illustrates the atomistic structure of pristine ZnO nanowires. The image is viewed from the $[2\bar{1}\bar{1}0]$ direction. The inset selected area electron diffraction (SAED) pattern confirms the [0001] growth direction of the nanowires.

2.2. In-situ experiments

In-situ TEM observations were carried out using the Nanofactory TEM-scanning tunneling microscopy (STM) holder inside a JEOL-2010 TEM. The electron flux dose rate was around 6×10^{19} e/(cm^2 s). The point resolution was 0.19 nm. A CCD camera (Gatan 894) was used for the digital recording of the TEM images. A typical exposure time was 0.2–1.0 s for each frame. The movies showing the *in-situ* lithiation processes in the supplementary materials were recorded by 2 frames per second. A few ZnO nanowires were attached to a gold (Au) rod with conductive silver epoxy as the working electrode. Li metal was scratched by an electrochemically shaped tungsten (W) tip inside a glove box. The Au and W tips were mounted on the station of TEM-STM holder. The assembly holder was loaded into the TEM chamber within a sealed plastic bag with an air exposure time less than 5 s. By manipulating the pizeo-driven stage with nanometer precision on the TEM-STM holder, the Li_2O covered Li metal came into contact with the single ZnO nanowire. Once a reliable contact was made, a bias voltage of −3 V was applied to drive the lithiation reaction of the ZnO nanowire. By accurately controlling the W tip toward the lithiated nanowire, a junction was formed using *in-situ* electron beam induced deposition (EBID) between the lithiated nanowire and the W tip. Uniaxial tension was applied to the lithiated nanowire by a controlled displacement to pull the W tip away from the nanowire. Fracture surface of lithiated nanowires was directly observed from the serial TEM images. *In-situ* bending experiments of individual nanowires before and after lithiation were performed by moving the W tip with a precision of 1 nm in the *X*- or *Y*-direction.

3. Results and discussion

Fig. 3(a) shows the schematic of the experimental setup of a nano-battery, consisting of a ZnO nanowire as the working electrode, Li/Li_2O as the counter electrode and the electrolyte, and Au and W rods as the current collectors. Precautions were taken to avoid the beam effects on lithiation reactions (Zhang et al., 2014a). *In-situ* experiments are carried out with a low dose rate of electron flux. During the entire experiments, the electron beam is distributed to a large illumination area with the diameter of 50 μm. We avoid the focus of beams to a small area that may induce undesired radiation effects. Similar experimental setup was also reported by other groups (Karki et al., 2013; Gu et al., 2013; McDowell et al., 2013; Wang et al., 2012; Liu et al., 2012). Fig. 3(b) shows the integrated nanowire at the initial state. When a bias voltage of −3 V is applied to the nanowire against Li, the reaction front propagates primarily along the longitudinal direction of the nanowire. After lithiation, the reacted part is elongated ~50% and the diameter expands ~30%. The total volume expansion was estimated about 150%. The longitudinal swelling of the nanowire is constrained. The constrained deformation causes bending of the nanowire. As shown in Fig. 3(c), bending is localized at the lithiated end, indicating that the lithiated phase is significantly more compliant than the pristine material. The time evolution of a single nanowire during lithiation is shown in the supplementary Movie 1.

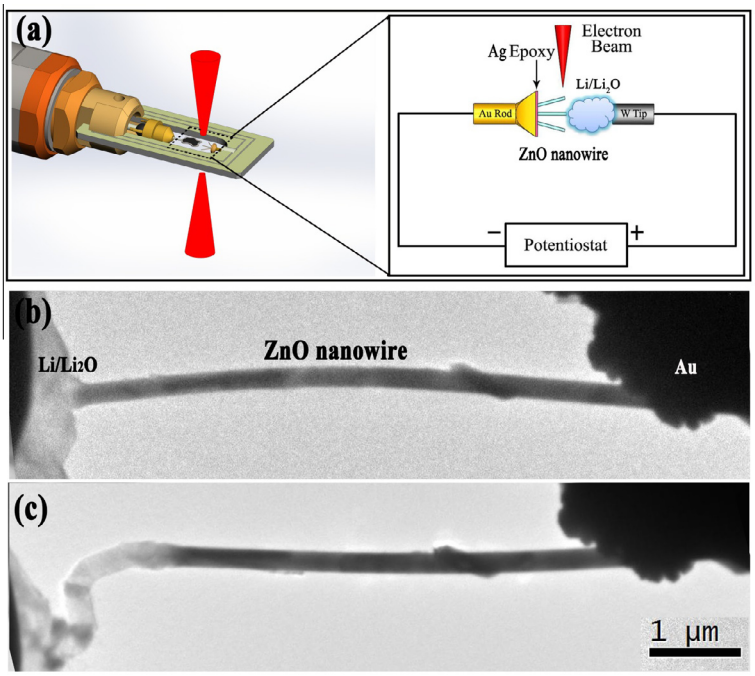

Fig. 3. (a) Schematic of a nano-battery consisting of a ZnO nanowire as the working electrode, Li/Li_2O as the counter electrode and the electrolyte. Au and W rods are current collectors. (b) A single ZnO nanowire integrated in the nano-battery. (c) Morphological change of the nanowire during the first lithiation. The constrained swelling causes dramatic bending at the lithiated end.

Previous studies on the reaction mechanism between Li and ZnO are informative (Liu et al., 2009; Wang et al., 2009; Su et al., 2013; Yang et al., 2013; Wu and Chang, 2013; Bresser et al., 2013). Upon lithiation, ZnO undergoes a two-step reaction. Li first converts the oxide into metallic Zn, leaving Zn nanoparticles dispersed in the amorphous matrix of Li_2O and Li–Zn–O alloys. Li further alloys with Zn to form Li–Zn compounds. We identify the phase evolution along the reaction path by performing electron diffraction analysis. We mark four areas, I, II, III, and IV, in Fig. 4(a), and the corresponding diffraction patterns are shown in Fig. 4(b). Overall, we see a transition from an amorphous matrix with polycrystalline phases to the single crystalline zone along the lithiation path. In the reacted parts, I, II, and III, the reaction products crystalline Zn, LiZn, Li_2O, and residual ZnO are dispersed in the amorphous matrix. The decreasing intensity of the amorphous halos implies gradually lower degree of lithiation along the reaction path.

While there is little debate on the final products of lithiated ZnO, the fundamental mechanism of the reaction pathway remains elusive. For example, how does metallic Zn nanocrystals aggregate and grow in the course of lithiation? Does the inhomogeneous dispersion of the metallic particles impair the propagation of lithiation? To answer the questions, we closely monitor the structural evolution together with the migration of the reaction front as a function of time. We use the diffraction patterns in Fig. 4 to identify the location of the reaction front. Fig. 5(a)–(f) show the propagation of the lithiation front in a single ZnO nanowire. Fig. 5(g) plots the migration distance versus time. The nearly linear behavior in the major stage of lithiation indicates that the rate of lithiation is limited by short-range processes at the solid-state reaction front, such as breaking and forming atomic bonds, rather than by the long-range diffusion of Li through the amorphous matrix. Such a rate-limiting process is a norm in heterogeneous reactions involving crystalline materials (Zhao et al., 2012; Cubuk et al., 2013; Yang et al., 2012). We note that the size of Zn nanoparticles steadily increases as lithiation proceeds. At a critical size, the nanocrystals will largely block the path of Li transport, and reduce the propagation velocity of the reaction front, as shown in the inset snapshot of Fig. 5(g).

The retardation of the reaction front by Zn nanocrystals originates from the thermodynamically unfavorable Li intercalation into Zn. We employ first-principles computational methods to compare the energetics of Li insertion into Zn and ZnO crystal lattices. Calculations based on Density Functional Theory are performed using Vienna Ab-initio Simulation Package (VASP). Projector-augmented-wave potentials are used to mimic the ionic cores, while the generalized gradient approximation in the Perdew–Burke–Ernzerh flavor is employed for the exchange and correlation functional (Kresse and Furthmüller, 1996; Kresse and Joubert, 1999). In particular, we treat $1s^2 2s^1$ orbitals as the valance configuration for Li. The atomic structures and system energy are calculated with an energy cutoff of 500 eV. The energy optimization is considered complete when the magnitude of the force on each atom is smaller than 0.02 eV $Å^{-1}$. A unit cell of Zn with the hexagonal close packed (HCP) structure is constructed containing 16 atoms. The lattice parameters are a = 5.27 Å, b = 4.56 Å, c = 10.32 Å. The unit cell of wurtzite

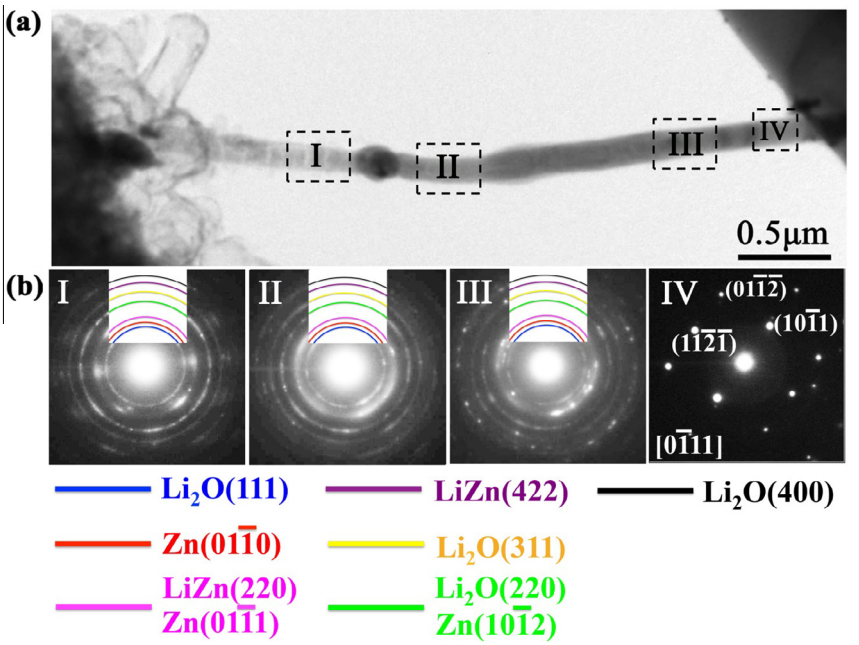

Fig. 4. A transition from the amorphous phase to the single crystalline zone along the lithiation path. Four areas are marked in (a). The corresponding diffraction patterns indicate that the reaction products crystalline Zn, LiZn, Li_2O, and residual ZnO are dispersed in the amorphous matrix. The decreasing intensity of the amorphous halos implies gradually lower degree of lithiation along the reaction path. The diffraction patterns are used to identify the location of the reaction front.

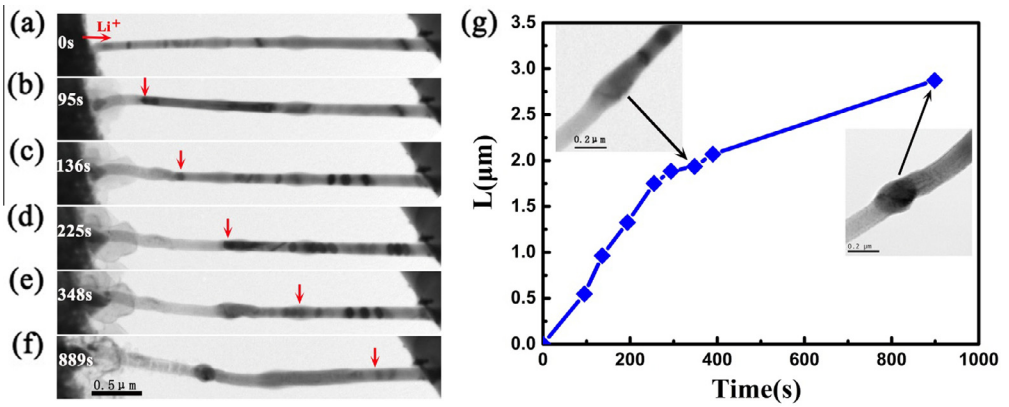

Fig. 5. (a)–(f) show the propagation of the lithiation front in a single ZnO nanowire during the first lithiation. (g) The migration distance of the reaction front as a function of time. The nearly linear behavior in the major stage of lithiation indicates the rate-limiting step dominated by the interfacial reaction, rather than by the long-range diffusion of Li through the amorphous matrix. The propagation of reaction front is impeded at a critical size of aggregated Zn nanoparticles, as shown in the inset snapshot.

ZnO contains 16 Zn atoms and 16 O atoms. The lattice parameters are $a = 6.57$ Å, $b = 5.68$ Å, $c = 10.62$ Å. Li insertion into a HCP structure is energetically favorable at the octahedral interstitial sites, Fig. 6 (Kushima et al., 2011; Huang et al., 2009). We compute the formation energy for a single Li insertion into the crystals. We take the energy of Zn/ZnO (E_{Zn}/E_{ZnO}) and the energy of a Li atom in its bulk form (E_{Li}) as the reference energies, with E_{Li-Zn}/E_{Li-ZnO} being the total energy of the system containing one Li in the cell. The formation energy E_f is calculated as $E_f = E_{Li-Zn/Li-ZnO} - E_{Zn/ZnO} - E_{Li}$. The formation energies for a single Li in ZnO and Zn are −0.07 eV and 0.15 eV. Apparently the structure of lithiated ZnO is thermodynamically more stable and alloying of Li with Zn is energetically unfavorable. In addition, we find the partial molar volume of Li in ZnO and Zn as $\Omega_{Li\ in\ ZnO} = 9.96$ Å^3 and $\Omega_{Li\ in\ Zn} = 28.54$ Å^3, respectively. The large discrepancy also indicates that Li intercalation in Zn lattice is less comfortable that the unit cell has to be largely stretched to accommodate the guest species. The simple calculation shows a qualitative comparison of the thermodynamic driving forces of lithiation in Zn and the oxide. A systematic

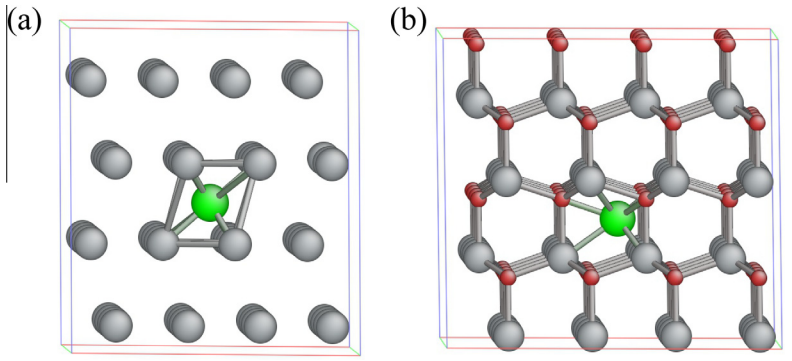

Fig. 6. Atomic structures of bulk Zn, (a), and ZnO, (b). Li insertion is energetically favorable at the octahedral interstitial sites. The grey, red, and green spheres represent the Zn, O, and Li atoms, respectively. (For interpretation of the references to color in this figure legend, the reader is referred to the web version of this article.)

analysis of the energetics and evolution of atomistic structures at higher Li contents warrants further careful studies. Nevertheless, the computation at low Li concentration provides insight on the sluggish lithiation reaction in Zn, which is relevant to the experimental observation that the aggregation of Zn nanocrystals reduces the migration velocity of the reaction front.

More interestingly, lithiation of ZnO exemplifies mechanical stress-regulated electrochemical reactions. Radial lithiation of a ZnO nanowire forms a structure of lithiated shell and unlithiated core. A field of stress is associated with the core–shell geometry. The lithiated phase develops tensile stresses, potentially causing surface fracture and facilitating Li transport through the crack surfaces. On the contrary, a material element in the unlithiated core is under a field of compressive stress, retarding the local electrochemical reaction. To illustrate the distinct feature of stresses, we consider a partially lithiated ZnO nanowire with its cross-section shown in Fig. 7. We derive the stress field using the continuum theory of finite deformation. We first note that, in order to accommodate a large volumetric strain of 150%, lithiated ZnO must deform plastically (Zhao et al., 2011, 2012; Nadimpalli et al., 2013). We represent a material element

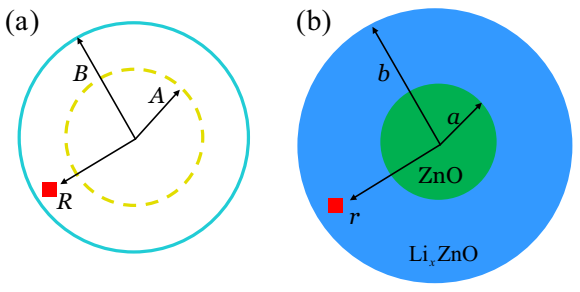

Fig. 7. Cross section of the core–shell structure of a ZnO nanowire during lithiation. (a) In the reference state, an element of lithiated ZnO is represented by its distance from the center R. The radius of the unlithiated ZnO (core) is A, and the radius of the lithiated phase (shell) B. (b) At time t, ZnO in the shell between the radii A and a is lithiated, and the element R moves to a new position of radius r.

in the reference configuration by its distance R from the center, Fig. 7(a). At time t, the material element moves to a place at a distance r from the center, Fig. 7(b). The function $r(R,t)$ specifies the deformation kinematics. Due to the mechanical constraint imposed by the crystalline ZnO in the axial direction, the lithiated phase is assumed to deform under the plane-strain conditions.

To focus on the main feature, we neglect the elasticity of the lithiated material; we model the lithiated phase as a rigid-plastic material with yield strength σ_Y. Consequently, the expansion of the shell is entirely due to lithiation. Consider the shell of the lithiated phase between the radii A and R. After lithiation, the core radius becomes a, and the material element moves to a new position r. We assume that Li is injected slowly and has sufficient time to diffuse through the lithiated region. The ratio of the volume of the lithiated shell over the volume of pristine phase is represented as β. Thus,

$$R^2 - A^2 + \beta(a^2 - A^2) = r^2 - a^2. \tag{1}$$

This equation gives the function $r(R,t)$ once the kinetics of the reaction front propagation $a(A)$ is prescribed. We write $f(A) = (1+\beta)(a^2 - A^2)$. Therefore $f(A)$ fully specifies the kinematics of the lithiated shell,

$$r = \sqrt{R^2 + f(A)}. \tag{2}$$

The stretches can be calculated as

$$\lambda_r = \frac{\partial r}{\partial R} = \frac{R}{r}, \quad \lambda_\theta = \frac{r}{R}, \quad \lambda_z = 1. \tag{3}$$

By neglecting the elastic deformation of the lithiated phase, the total expansion is only accommodated by the plastic deformation. We calculate the strain components from the stretches,

$$\varepsilon_r^p = \varepsilon_r = \log\lambda_r, \quad \varepsilon_\theta^p = \varepsilon_\theta = \log\lambda_\theta, \quad \varepsilon_z^p = \varepsilon_z = \log\lambda_z. \tag{4}$$

To calculate the stress field, one has to consider the incremental plastic deformation with respect to time. Given Eqs. (3) and (4), we obtain that

$$\delta\varepsilon_r^p = -\frac{1}{2r^2}\delta f, \quad \delta\varepsilon_\theta^p = \frac{1}{2r^2}\delta f, \quad \delta\varepsilon_z^p = 0. \tag{5}$$

The equivalent plastic strain increment is

$$\delta\varepsilon^p_{eq} = \sqrt{\frac{2}{3}\delta\varepsilon^p_{ij}\delta\varepsilon^p_{ij}} = \frac{2}{\sqrt{3}r^2}\delta f. \tag{6}$$

We adopt the flow rule

$$s_{ij} = \frac{2}{3}\frac{\sigma_Y}{\delta\varepsilon^p_{eq}}\delta\varepsilon^p_{ij}. \tag{7}$$

where s_{ij} is the deviatoric stress, defined as $s_{ij} = \sigma_{ij} - \frac{1}{3}\sigma_{ii}$. Therefore,

$$s_r = -\frac{\sqrt{3}}{3}\sigma_Y, \quad s_\theta = \frac{\sqrt{3}}{3}\sigma_Y, \quad s_z = 0. \tag{8}$$

and

$$\sigma_r - \sigma_\theta = s_r - s_\theta = -\frac{2\sqrt{3}}{3}\sigma_Y. \tag{9}$$

Consider the force balance of a material element in lithiated ZnO

$$\frac{\partial\sigma_r}{\partial r} + \frac{\sigma_r - \sigma_\theta}{r} = 0, \tag{10}$$

the radial stress can be obtained by integrating Eq. (10), it gives,

$$\sigma_r = \frac{2\sqrt{3}}{3}\sigma_Y \log r + D. \tag{11}$$

The integration constant D is determined by the traction-free boundary condition, $\sigma_r(b,t) = 0$, such that

$$\begin{aligned}
\sigma_r &= \frac{2\sqrt{3}}{3}\sigma_Y \log\frac{r}{b} \\
\sigma_\theta &= \frac{2\sqrt{3}}{3}\sigma_Y\left(\log\frac{r}{b} + 1\right) \\
\sigma_z &= \frac{2\sqrt{3}}{3}\sigma_Y\left(\log\frac{r}{b} + \frac{1}{2}\right).
\end{aligned} \tag{12}$$

The stress field in the elastic core ($0 \leqslant r \leqslant a$) can be solved using the familiar solution of Lamé problem (Timoshenko and Goodier, 1970), it gives,

$$\begin{aligned}
\sigma_r = \sigma_\theta &= \frac{2\sqrt{3}}{3}\sigma_Y \log\frac{a}{b} \\
\sigma_z &= \frac{4\sqrt{3}}{3}\nu\sigma_Y \log\frac{a}{b}
\end{aligned} \tag{13}$$

where ν is the Poisson's ratio of ZnO. The stress field would be modified by the longitudinal propagation of the reaction front because of the presence of mismatch strain at the interface. Nevertheless, the key characteristics of tensile stresses in the lithiated shell and compressive stresses in the pristine core remain the same. As shown in the closed-forms (12) and (13), the surface of the lithiated shell is subject to tensile stresses in the hoop and axial directions, while a material element in the unlithiated core is under compressive stresses.

The mechanical stress contributes to the thermodynamic driving force of lithiation. In an example of crystalline Si, the mechanical energy even may counterbalance the electrochemical driving force of

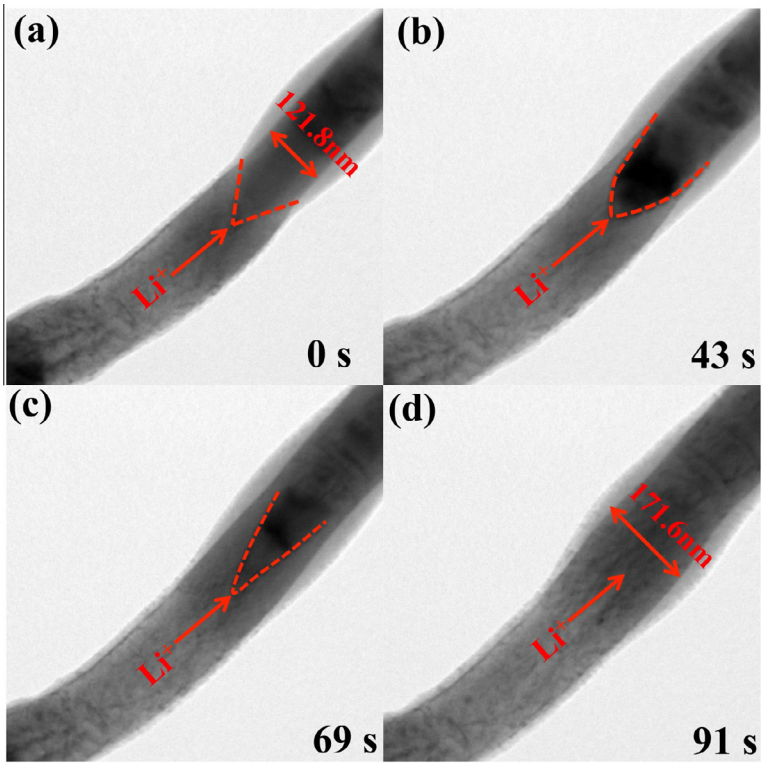

Fig. 8. Time evolution of the curved reaction front. The transition from tensile stresses in the lithiated shell to compressive stresses in the unlithiated core breaks the planar reaction front into a curved interface. The radius of curvature gradually decreases and the core is eventually lithiated as the reaction front propagates.

lithiation and causes stagnation of the reaction front (Zhao et al., 2012; McDowell et al., 2012). The change of free energy due to stresses associated with an electrochemical reaction can be written as $\Delta G_m = -\Omega\sigma_m$, where Ω represents the partial molar volume of Li, and σ_m the hydrostatic stress. A negative ΔG_m facilitates lithiation. As expected, a tensile mean stress in the lithiated shell promotes lithiation, and a compressive mean stress in the unlithiated core retards lithiation. The asymmetry of stresses in ZnO nanowires breaks the planar reaction front into a curved interface which is a phenomenon similar to the Mullins–Sekerka instability for a moving liquid–solid interface (Mullins and Sekerka, 1964). Fig. 8 shows the time evolution of the curved SSRF. The magnitude of compressive stresses increases toward the core, dictating a gradually decreasing driving force of lithiation from the surface to the center of the nanowire. The pattern of the reaction front shown in Fig. 8 corroborates the transition of the stress state. The radius of curvature gradually decreases and the core is eventually lithiated as the reaction front propagates. Another noteworthy feature is the surface fracture induced by the tensile stresses in the lithiated phase. Fig. 9 shows discrete surface cracks in the selected regions in front of the reaction interface. The crack surfaces provide fast channels for Li penetration that divides the nanowire into multiple segments of glassy domains (Kushima et al., 2011). Micro-cracks also exist in the reacted parts; however, the crack morphologies are not as visible due to the large volumetric swelling. Surface fracture of lithiated ZnO and their complex interplay with the process of lithiation was extensively investigated in a previous study (Kushima et al., 2011). This interesting phenomenon is not the focus of present study.

Lithiation results in dramatic changes of the mechanical properties of ZnO nanowires. Significant embrittlement associated with lithiation has been observed in a variety of materials; ZnO obeys this trend as well (Liu et al., 2011; Zhao et al., 2011). We perform *in-situ* uniaxial tension experiments to a lithiated ZnO nanowire that lithiated region and unlithiated part coexist. Such a partially lithiated material provides direct contrast of fracture strength of the pristine structure versus the lithiated phase. Fig. 10(a)–(e) show the snapshots of the nanowire during uniaxial deformation. By repeating the experiments on several nanowires, fracture exclusively occurs in the lithiated zone. Such an observation indicates that the fracture strength of lithiated ZnO is lower than that in pure ZnO. Fig. 10(f)–(g) illustrates the brittle failure of lithiated region with sharp fracture edges. Kushima et al. performed first-principles calculations and found that the elastic modulus drops by about factor of two from ZnO to $Li_{0.25}ZnO$ (Kushima et al., 2011). By assuming the same failure strain ~0.2% for both ZnO and its lithiated form, we may estimate that the fracture strength of ZnO nanowires decreases at least by factor of two upon lithiation. Supplementary Movies 2 and 3 shows the other comparison of mechanical behaviors in the two material states by performing *in-situ* bending experiments. It clearly

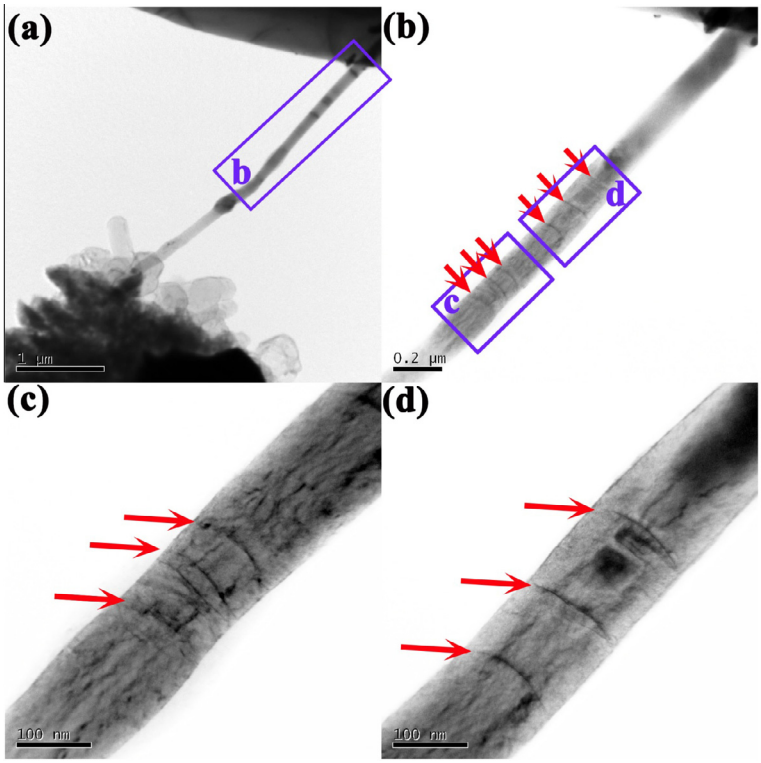

Fig. 9. Surface cracks observed at the selected areas (b)–(d) on the (0001) basal plane of ZnO nanowires.

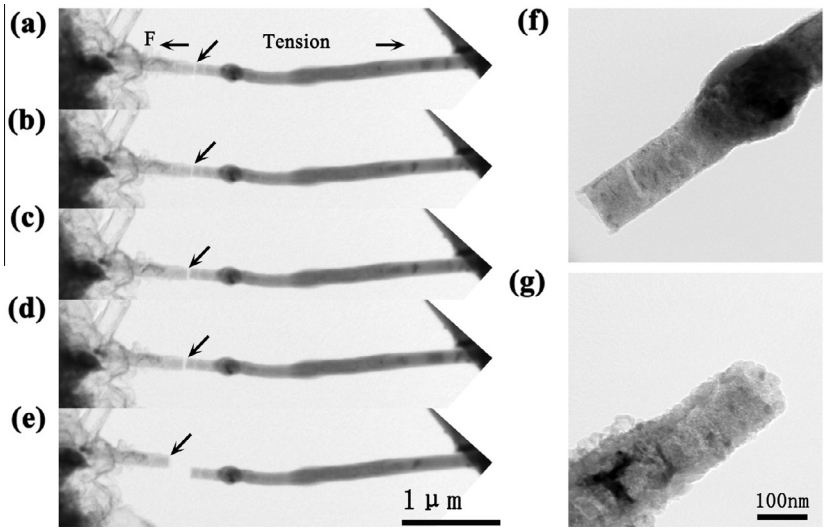

Fig. 10. *In-situ* uniaxial tensile deformation of a lithiated ZnO nanowire. The nanowire is partially lithiated as shown in Fig. 5(f). Fracture occurs in the lithiated zone, indicating a lower tensile strength of the lithiated phase in comparison with that of the pristine material. (f) and (g) Fracture surface of the nanowire shows the feature of brittle failure.

demonstrates the dramatic change from the pristine material with resilient elasticity to a fragile structure in the lithiated form.

4. Conclusions

We study the lithiation behavior of ZnO nanowires using complementary *in-situ* transmission electron microcopy experiments, continuum theories, and first-principles computation. From the standpoint of mechanics, ZnO is a model system to understand the intimate coupling between electrochemistry and mechanics, that is, electrochemical reactions induce a field of stress and often lead to mechanical degradation of the lithiated material, meanwhile, the stress field significantly influences the thermodynamics and kinetics of the chemical reactions. ZnO illustrates such features that tensile stresses in the lithiated shell cause discrete surface fractures and facilitate Li transport, while compressive stresses in the unlithiated core retard the local electrochemical reaction. The asymmetry of the stress field breaks the planer solid-state reaction front into a curved interface that is a reminiscence of the well-established Mullins–Sekerka instability for a moving liquid–solid interface. In addition, we observe that metallic Zn nanoparticles aggregate in the conversion reaction of ZnO. At a critical size, Zn nanoparticles will largely block the path of Li transport and reduce the migration velocity of the reaction front due to the thermodynamically unfavorable lithiation reaction. The inhomogeneous dispersion and growth of metallic nanocrystals is a generic phenomenon for oxides electrodes in Li-ion batteries (Huang et al., 2010; Su et al., 2013; Wang et al., 2013). The findings reported here are relevant to other electrochemical systems involving oxides and provide fundamental perspectives on the chemomechanical behaviors of high-capacity electrodes at the intrinsic scales.

Acknowledgements

Y.Z. acknowledges the National Natural Science Foundation – China funded project (11374027), Beijing Natural Science Foundation (2132014), and Special Projects for Development of National Major Scientific Instruments and Equipment (2012YQ03007508). The research project is supported by the start-up funds at Purdue University. K.Z. is grateful for the support of Haythornthwaite Foundation Initiation Grant from American Society of Mechanical Engineering – United States.

Appendix A. Supplementary data

Supplementary data associated with this article can be found, in the online version, at http://dx.doi.org/10.1016/j.mechmat.2015.05.004.

References

Bian, X.-C., Huo, C.-Q., Zhang, Y.-F., Chen, Q., 2008. Preparation and photoluminescence of ZnO with nanostructure by hollow-cathode discharge. Front. Mater. Sci. Chin. 2, 31–36.

Bresser, D. et al., 2013. Transition-metal-doped zinc oxide nanoparticles as a new lithium-ion anode material. Chem. Mater. 25, 4977–4985.

Chunqing, H., Yuefei, Z., Fuping, L., Qiang, C., Yuedong, M., 2009. Different shapes of nano-ZnO crystals grown in catalyst-free DC Plasma. Plasma Sci. Technol. 11, 564.

Cubuk, E.D. et al., 2013. Morphological evolution of Si nanowires upon lithiation: A first-principles multiscale model. Nano Lett. 13, 2011–2015.

Favors, Z. et al., 2014. Stable cycling of SiO_2 nanotubes as high-performance anodes for lithium-ion batteries. Sci. Rep. 4, 4605.

Gu, M. et al., 2013. Electronic origin for the phase transition from amorphous Li*x*Si to crystalline $Li_{15}Si_4$. ACS Nano 7, 6303–6309.

Haftbaradaran, H., Gao, H.J., Curtin, W.A., 2010. A surface locking instability for atomic intercalation into a solid electrode. Appl. Phys. Lett. 96, 091909.

Huang, G.-Y., Wang, C.-Y., Wang, J.-T., 2009. First-principles study of diffusion of Li, Na, K and Ag in ZnO. J. Phys.: Condens. Matter 21, 345802.
Huang, J.Y. et al., 2010. In situ observation of the electrochemical lithiation of a single SnO_2 nanowire electrode. Science 330, 1515–1520.
Jiang, J. et al., 2012. Recent advances in metal oxide-based electrode architecture design for electrochemical energy storage. Adv. Mater. 24, 5166–5180.
Karki, K. et al., 2013. Hoop-strong nanotubes for battery electrodes. ACS Nano 7, 8295–8302.
Kresse, G., Furthmüller, J., 1996. Efficient iterative schemes for ab initio total-energy calculations using a plane-wave basis set. Phys. Rev. B 54, 11169.
Kresse, G., Joubert, D., 1999. From ultrasoft pseudopotentials to the projector augmented-wave method. Phys. Rev. B 59, 1758.
Kushima, A. et al., 2011. Leapfrog cracking and nanoamorphization of ZnO nanowires during in situ electrochemical lithiation. Nano Lett. 11, 4535–4541.
Li, H., Huang, X., Chen, L., 1999. Anodes based on oxide materials for lithium rechargeable batteries. Solid State Ionics 123, 189–197.
Liu, J. et al., 2009. Carbon/ZnO nanorod array electrode with significantly improved lithium storage capability. J. Phys. Chem. C 113, 5336–5339.
Liu, Y. et al., 2011. Lithiation-induced embrittlement of multiwalled carbon nanotubes. ACS Nano 5, 7245–7253.
Liu, X.H. et al., 2012. In situ atomic-scale imaging of electrochemical lithiation in silicon. Nat. Nanotechnol. 7, 749–756.
McDowell, M.T. et al., 2012. Studying the kinetics of crystalline silicon nanoparticle lithiation with in situ TEM. Adv. Mater. 24, 6034–6041.
McDowell, M.T. et al., 2013. In situ TEM of two-phase lithiation of amorphous silicon nanospheres. Nano Lett. 13, 758–764.
Mullins, W.W., Sekerka, R., 1964. Stability of a planar interface during solidification of a dilute binary alloy. J. Appl. Phys. 35, 444–451.
Nadimpalli, S.P. et al., 2013. On plastic deformation and fracture in Si films during electrochemical lithiation/delithiation cycling. J. Electrochem. Soc. 160, A1885–A1893.
Pharr, M., Zhao, K.J., Wang, X.W., Suo, Z.G., Vlassak, J.J., 2012. Kinetics of initial lithiation of crystalline silicon electrodes of lithium-ion batteries. Nano Lett. 12, 5039–5047.
Service, R.F., 2014. Tanks for the batteries. Science 344, 352–354.
Su, Q., Dong, Z., Zhang, J., Du, G., Xu, B., 2013. Visualizing the electrochemical reaction of ZnO nanoparticles with lithium by in situ TEM: two reaction modes are revealed. Nanotechnology 24, 255705.
Tang, M., Belak, J.F., Dorr, M.R., 2011. Anisotropic phase boundary morphology in nanoscale olivine electrode particles. J. Phys. Chem. C 115, 4922–4926.
Tao, L.Q. et al., 2012. Co_3O_4 nanorods/graphene nanosheets nanocomposites for lithium ion batteries with improved reversible capacity and cycle stability. J. Power Sources 202, 230–235.
Timoshenko, S., Goodier, J.N., 1970. Theory of Elasticity, third ed. Mcgraw-Hill College, Blacklick, OH).
Van Noorden, R., 2014. A better battery. Nature 507, 26–28.
Wan, J. et al., 2014. Two dimensional silicon nanowalls for lithium ion batteries. J. Mater. Chem. A 2, 6051–6057.
Wang, H., Pan, Q., Cheng, Y., Zhao, J., Yin, G., 2009. Evaluation of ZnO nanorod arrays with dandelion-like morphology as negative electrodes for lithium-ion batteries. Electrochim. Acta 54, 2851–2855.
Wang, J.W. et al., 2012. Sandwich-lithiation and longitudinal crack in amorphous silicon coated on carbon nanofibers. ACS Nano 6, 9158–9167.
Wang, L. et al., 2013. Real-time in situ TEM studying the fading mechanism of tin dioxide nanowire electrodes in lithium ion batteries. Sci. Chin. Technol. Sci. 56, 2630–2635.
Wu, M.-S., Chang, H.-W., 2013. Self-Assembly of NiO-coated ZnO nanorod electrodes with core–shell nanostructures as anode materials for rechargeable lithium-ion batteries. J. Phys. Chem. C 117, 2590–2599.
Yang, H. et al., 2012. Orientation-dependent interfacial mobility governs the anisotropic swelling in lithiated silicon nanowires. Nano Lett. 12, 1953–1958.
Yang, G., Song, H., Cui, H., Liu, Y., Wang, C., 2013. Ultrafast Li-ion battery anode with superlong life and excellent cycling stability from strongly coupled ZnO nanoparticle/conductive nanocarbon skeleton hybrid materials. Nano Energy 2, 579–585.
Yang, H. et al., 2014. A chemo-mechanical model of lithiation in silicon. J. Mech. Phys. Solids 70, 349–361.
Yu, H.C. et al., 2014. Designing the next generation high capacity battery electrodes. Energy Environ. Sci. 7, 1760–1768.
Zhang, W.J., 2011. Lithium insertion/extraction mechanism in alloy anodes for lithium-ion batteries. J. Power Sources 196, 877–885.
Zhang, Y., Li, Y., Wang, Z., Zhao, K., 2014a. Lithiation of SiO_2 in Li-ion batteries: in-situ transmission electron microscopy experiments and theoretical studies. Nano Lett. 14, 7161–7170.
Zhang, L., Wu, H.B., Lou, X.W.D., 2014b. Iron-oxide-based advanced anode materials for lithium-ion batteries. Adv. Energy Mater. 4, 1300958.
Zhao, K.J., Pharr, M., Cai, S.Q., Vlassak, J.J., Suo, Z.G., 2011. Large plastic deformation in high-capacity lithium-ion batteries caused by charge and discharge. J. Am. Ceram. Soc. 94, S226–S235.
Zhao, K.J., Pharr, M., Vlassak, J.J., Suo, Z.G., 2011. Inelastic hosts as electrodes for high-capacity lithium-ion batteries. J. Appl. Phys. 109, 016110.
Zhao, K.J. et al., 2011. Lithium-assisted plastic deformation of silicon electrodes in lithium-Ion batteries: A first-principles theoretical study. Nano Lett. 11, 2962–2967.
Zhao, K., Pharr, M., Hartle, L., Vlassak, J.J., Suo, Z., 2012. Fracture and debonding in lithium-ion batteries with electrodes of hollow core-shell nanostructures. J. Power Sources 218, 6–14.
Zhao, K.J. et al., 2012. Concurrent reaction and plasticity during initial lithiation of crystalline silicon in lithium-ion batteries. J. Electrochem. Soc. 159, A238–A243.
Zhao, K.J. et al., 2012. Reactive flow in silicon electrodes assisted by the insertion of lithium. Nano Lett. 12, 4397–4403.